Structural, Morphological, Topographical Characterization of Titanium Dioxide Nanotubes Metal Substrates for Solar Cell Application

Mpheleki Lupiwana[1,2], Raymond Taziwa[1,2,*], Edson Meyer[1] and David Katwire[2]

[1]*Fort Hare Institute of Technology (FHIT), University of Fort Hare, Private Bag X1314, Alice, 5700, Republic of South Africa*

[2]*Chemistry Department, University of Fort Hare, Private Bag X1314, Alice, 5700, Republic of South Africa*

Abstract: High demand on energy conversion in DSSC, requires development of well-organized TiO_2 nanotube structures because of their large surface area-to-volume ratio, superior lifetime and provision of optimal pathways for electron percolation. In this work multi-layered Titanium dioxide nanotubes (MTNTs) have been fabricated by an electrochemical anodization technique. MTNTs were annealed at 350°C, 450°C, 550°C and 650°C. The structural and morphological properties of the MTNTs have been evaluated by XRD, Confocal Raman Microscopy (CRM) through Large Area Scan (LAS), Depth Profiling (DP) and SEM analysis. SEM-EDX has been employed for element elucidation of TNTs. SEM analysis has revealed the change in surface with increase in annealing temperature. Moreover SEM analysis has revealed the presence of porous and MTNTs for the samples annealed at 350°C and 650°C with modal pore size of 35.56 nm and 31.05 nm respectively. EDX analysis has revealed that the fabricated MTNTs consist of Ti and O atoms. CRM has confirmed the presence of Anatase phase TiO_2 with Raman vibration modes at 142.37 cm^{-1}, 199.04 cm^{-1}, 394.67 cm^{-1}, 516.16 cm^{-1} and 639.29 $cm^{-1}$with the Rutile phase TiO_2 with Raman vibration modes at 445.26 cm^{-1} and 612.07 cm^{-1}. The XRD analysis has revealed that the MTNTs consist of multiphase Anatase and Rutile phase depending on the annealing temperature. AFM has confirmed the existence of porous nano-tubular structure for all samples.

Keywords: Titanium dioxide, electro-anodization, confocal Raman Spectroscopy large area scan and depth profiling.

INTRODUCTION

Ordered titanium dioxide (TiO_2) nanostructures, more specifically TiO_2 nanotubes (TNTs) and TiO_2 nanoparticles (TNPs), have received a great of attention in recent years because of their application as effective carrier transporters in dye-sensitized solar cells (DSSCs) [1, 3]. Substantial efforts have been focused on fabrication of well aligned TNTs. One dimensional and highly ordered nanotubes architecture offers excellent electrical channel for vectorial charge transfer so that photo induced electron hole pairs can be effectively separated, which minimizes recombination and maximizes photo absorption. In comparison with the randomly packed and disordered TNPs networks with numerous particle-particle interfaces, TNTs arrays with highly ordered vertically oriented nanotubular structures provides a larger internal surface area and at the same time introduce a free electron traveling path to reduce carrier recombination possibilities [4]. To further enhance vectorial charge transfer activity TNT arrays, various strategies have been employed such as the improvement of surface morphology, crystal structure, surface area [5, 10], introduction of heterogeneous structures by decoration [11, 19] and doping with non-metal [20, 26] or metal elements [27, 32]. Amongst these, the enhancement of TNTs crystallinity has been considered as an important and widely investigated approach to achieve better vectorial electron transport in DSSCs [33]. Recent studies have demonstrated that the electron transport in typical TNTs is as slow as that in TNP films, even though the underlying mechanisms are quite different (exciton-like trap states in TNT films and structural disorder in TNP films) [34, 36]. As a result of the existence of these states, which suppresses the electron mobility, the improvement of TNT based DSSCs is limited and the highest efficiency of DSSCs consisting of the pure TNTs (without further surface treatment) is only about 5% (around 7-9% for mixed systems), which is still lower than that achieved with the TNPs [37, 38]. Crystallization by annealing at high temperature in oxidative atmosphere is an effective way to enhance the electron mobility in TNTs, since the annealing leads to lowered density of both bulk and surface trap states by reducing the number of defects and oxygen vacancies/Ti^{+3} existing in the band gap induced by amorphous domains, grain boundaries, and impurities embedded during anodization [35,39]. Characterization of TNT arrays continues to grow in importance and to impact the development of efficient

*Address correspondence to this author at the Fort Hare Institute of Technology (FHIT), University of Fort Hare, Private Bag X1314, Alice, 5700, Republic of South Africa; Tel: 040 602 2086; +27 83 351 1909;
E-mail: rtaziwa@ufh.ac.za

E-ISSN: 2410-4701/17

electrode materials for DSSCs. The development of efficient TNT electrode materials for solar cell applications requires detailed information about the structural, morphological, chemical and as well as topographical properties at nanometer scale. The inherent limitations of traditional characterization techniques such as the inability of these methods to chemically, morphologically and structurally differentiate with spatial resolution and without sophisticated sample preparation techniques have been the main challenge limiting the development of efficient solar cell devices employing TNT photo-anodes. Atomic Force microscopy (AFM) can provide spatial information along and perpendicular to the surface of the TNT substrates with resolution on the order of 1 nm. The most commonly used AFM imaging mode is the AC mode. In this AFM imaging mode the cantilever is oscillated at its resonance frequency and the topography of the surface is scanned by keeping the oscillation constant. Confocal Raman spectroscopy can be employed for the characterization of the chemical and structural (distinguish between phases) features of the TNT arrays. Raman spectroscopy then provides qualitative and quantitative information about the chemical nature and phase properties of TNT arrays. Most spectroscopy set up the spatial resolution is very poor because the excitation laser spot diameter is in the order of 100 μm. Optical microscopy, on the other hand, is capable of providing a spatial resolution down to 200 nm using visible light excitation. However, in confocal Raman microscopy, the light from the sample is detected through a pinhole at the back focal plane of the microscope, giving rise to depth resolution and a strongly reduced background signal to collect high resolution Raman images, the sample is scanned point by point and line by line. In this work to achieve the highest resolution confocal Raman Microscope (CRM) extended with AFM capabilities was used to differentiate or correlate the chemical, morphologically and structural properties of TNTs membranes and without sophisticated sample preparation. Moreover this work has presented for the first time combined confocal Raman-AFM system to structurally, chemically and topographically to evaluate the phase distribution of TNT arrays fabricated by electro-anodization technique.

2. EXPERIMENTAL

This section starts off by presenting in detail the experimental methods used in preparation of titanium substrates prior to anodization. We also present here the actual method used in the fabrication of TNTs membranes. Lastly we present here the characterization techniques used in the study.

2.1. Fabrication Procedure

Titanium foils (0.032 mm in thickness, 99.7 purity) from (Alfa Aesar) were cut into (1 × 1 cm) and were annealed at 500 °C for 1 hour. The annealed titanium foil were first sonicated with acetone for 15 minutes and polished. The polished titanium foils were cleaned

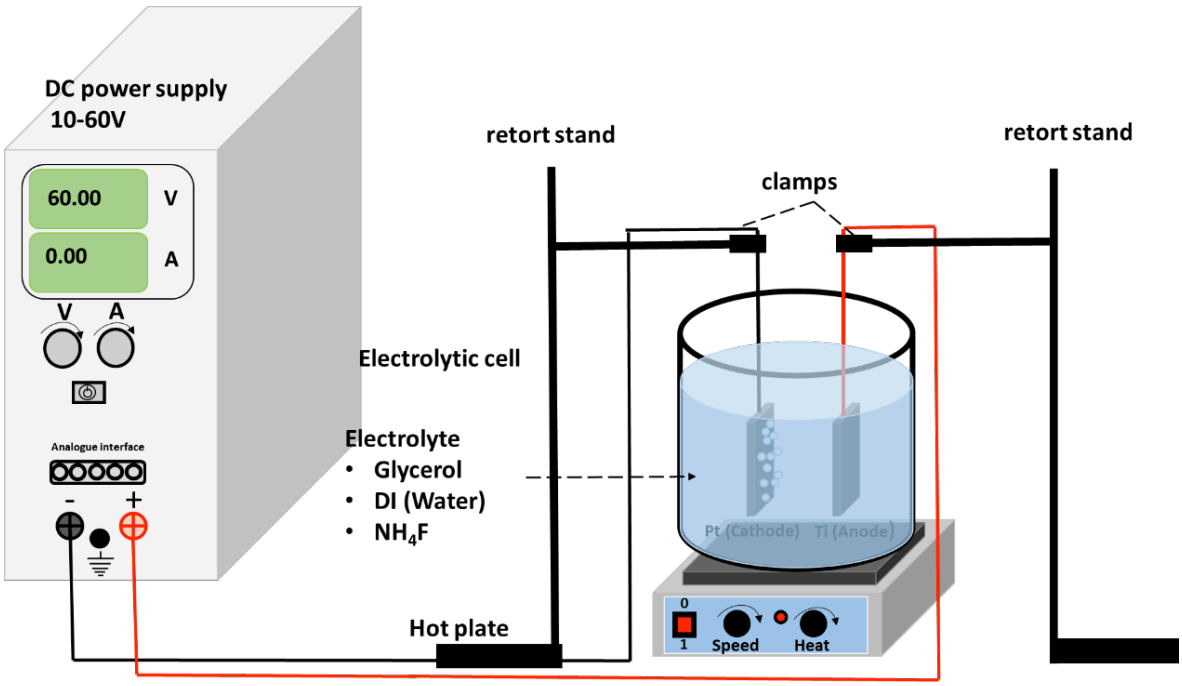

Figure 1: Schematic diagram of the electro-anodization system used for fabrication of TNTs membranes.

using sonicator (mrc ultrasonic cleaner) in deionized water, and acetone for 40 minutes each. The polished, cleaned titanium foils were allowed to dry in air for 5 minutes. For the back side insulation acrylic adhesive glue was applied to the back side so that only the front side faces the electrolyte. The as backside insulated titanium substrates were then dried under nitrogen gas. The self-organised TNTs were fabricated by anodization of Ti foils in the electrolyte consisting of Glycerol + 3 vol.% deionised water + 0.5 wt% ammonium fluoride (NH_4F). Anodization was performed in a two-electrode configuration connected to a DC power supply (PS 8000 T) with titanium foil as the working electrode and platinum foil as the counter electrode under constant 60V anodic potential for 12 hr at room temperature. Figure **1** shows the schematic presentation of the experimental set up used in the study. The fabricated TNTs membranes on a metal substrate were characterized without any detachment.

2.2. Characterizations

To obtain the crystallographic phase and associated parameters of TiO_2 samples of the synthesized TNTs, XRD spectra were obtained using a Bruker D8 Advance X-Ray diffractometer (XRD) with a Cu anode, generating Kά radiation of wavelength 1.544 Å and operating at 40 kV and 40 mA. Field Emission Scanning Electron Microscope (FE-SEM) Zeiss Auriga SEM equipped with EDS with SmartSEM software was used to study the elemental, structural and morphological properties of nanotubular TiO_2 with an accelerating voltage of 30 KV at different magnifications. In order to evaluate the thickness and cross sectional morphology of nanotubular TiO_2. For cross sectional and surface analysis the samples were frozen in liquid nitrogen and fractured whilst frozen. The fractured sample was then mounted onto a sample holder with the fractured side facing up after gold coating. For surface morphology the samples were mounted directly onto a sample stub and sputter coated. Structural characterization was also carried done by using confocal Raman microscopy coupled with an atomic force microscopy (AFM) instrument (Witec ALPHA 300RA) with a fiber coupled DPSS laser 532 nm with maximum output power after single mode fiber coupling of 44 mW was used as the excitation source Data was then collected using a multimode fiber into a high throughput lens based spectrograph (UHTS 300) with 300 mm focal length and two gratings 600 g/mm and 1800 g/mm, both blazed at 550 nm. The UHTS 300 spectrograph is connected with a peltier cooled back illuminated CCD camera with better than 90% QE in the visible excitation. RAMAN imaging was done using a 50X nikon objective, 0.55 NA. A total of 10,000 spectra were acquired with an integration time of 0.01s per spectrum". 1. The samples were mounted on a piezo-driven scan platform having a positioning accuracy of 4 nm (lateral) and 0.5 nm (vertical). The piezoelectric scanning table allows three-dimensional displacements in steps of 3 nm, giving a very high spatial resolution confocal Raman microscopy. For confocal Raman image scans, an entire RS spectrum is collected at over an image point. Each confocal Raman Image consisted of 526 x 526 points. The acquired spectra were processed and analysed using the Wi Project 4.1, which allows a specific, sensitive, and nonintrusive analysis of the spectra collection that is immune to interference and provides a method for characterizing chemical properties of heterogeneous samples with great resolution and rapid data collection.

3. RESULTS AND DISCUSSION

3.1. SEM-EDS Analysis

The electro-anodization of the titanium metal substrate to TNT proceeds by electric field-assisted oxidation of Ti metal to form TiO_2 In the first step. The first step involves the formation of an oxide barrier layer on the electrolyte-metal interface [40, 41].

$$Ti^{1+} + 2H_2O \rightarrow TiO_2 + 4H^+ \quad (1)$$

The second step proceeds with the dissolution of the compact anodic oxide that is formed in Eq. (1) It takes place simultaneously and only after a certain period of time does the growth of ordered nanotubular structures takes place according to Eq. **(2)**.

$$Ti^{1+} + 6F^- \rightarrow TiF_6^{2-}, \quad (2)$$

The presence of electric field results in formation nanotubes which is proceeded by formation of randomly distributed pits. The diffusion of the fluoride electrolyte in the presence of the electric field results in formation of cracks and slits this enhances the dissolution rate of the fluoride electrolyte. Formation of nanotubes is dependent on the diffusion of F^- ions through the cracked oxide barrier layer according to Eq. **(3)**.

$$TiO_2 + 6F^- + 4H^+ \rightarrow [TiF_6]^{-2} + 2H_2O \quad (3)$$

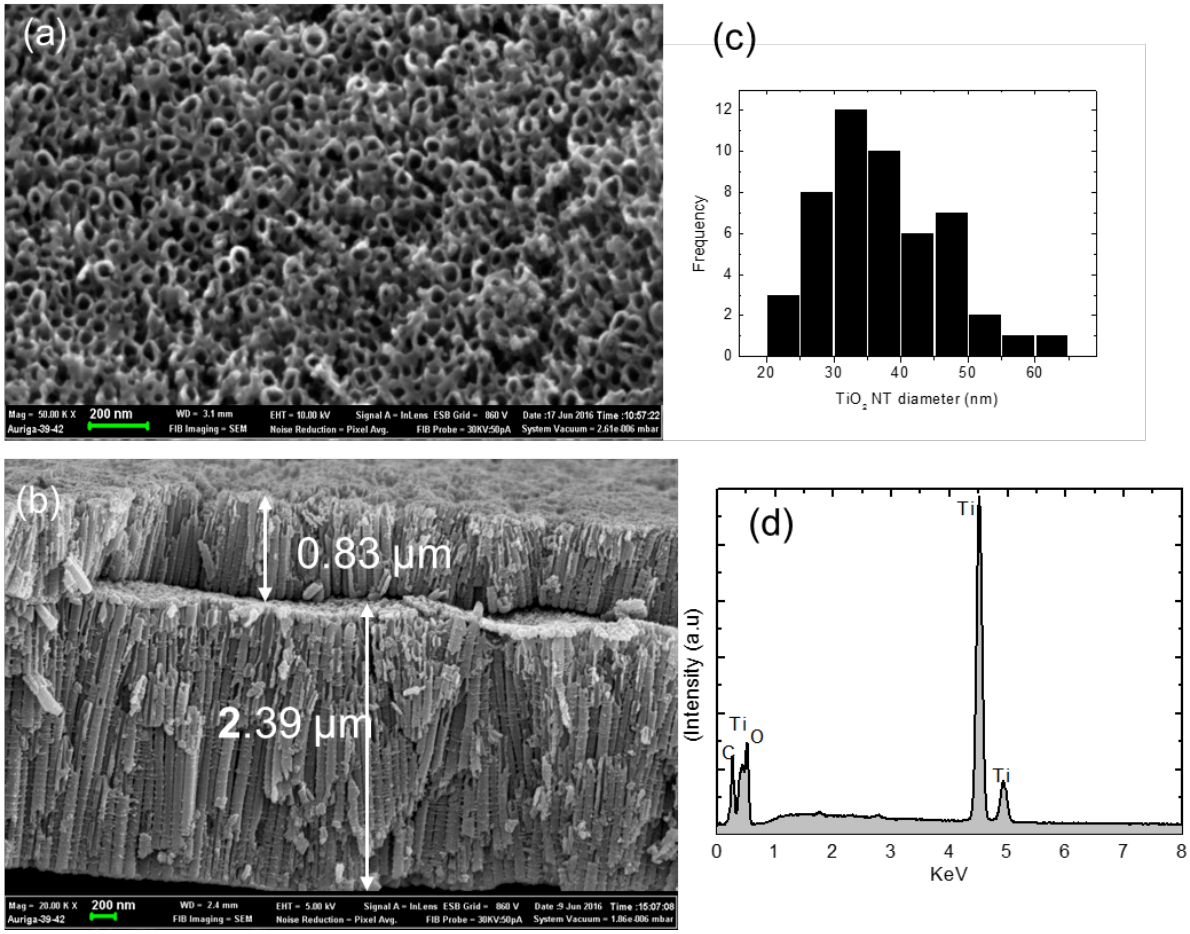

Figure 2: Field-emission scanning electron microscopy (FESEM) images of TNTs annealed at 350 ºC (**a**) surface SEM images of TNTs (**b**) cross sectional SEM images (**c**) Histogram showing pore size distribution (**d**) elemental composition via EDX.

The growth of TNT occurs by continuous etching of the oxide inside the nanotubes. In this work growth of TNTs occurred at an anodization voltage of 60V in the presence of a glycerol electrolyte solution containing 0.5 wt% NH_4F at room temperature. Figure **2(a)** shows the surface SEM micrographs of TNTs membranes annealed at 350 ºC. SEM micrographs clearly reveal nonporous layers with a with modal pore size of 34.56 nm.

The histogram in Figure **2(b)** shows the pore size distribution of between 20-70 nm for the TNTs annealed at 350 ºC. In addition Figure **2(c)** shows the cross sectional SEM micrographs revealed a Multi-layered TNTs array with an overall nanotube length of an 3.22 µm with top layer having a nanotube length of 0.83 µm and a bottom layer of 2.39 µm. also evident from the surface SEM micrograph in Figure **2(a)** is the presence of a nanoporous oxide layer covering some of the nanotube, according to theory, the nanotubular growth results from chemical etching in the presence of F^- ions Eq. **(3)** of the tube walls from both sides leading to formation of nanotube layers [42-45]. However the oxide layer on top of the nanotubes might be due to the first oxide layer formed from Eq. **(1)**. It can be explained that the nanoporous oxide layer was not completely dissolved during the etching process from Eq. **(2)** hence the nanotubes are not completely separated from each other [46, 47]. This oxide layer is also evident from the SEM micrograph in Figure **2(b)**. In addition the cross sectional SEM Figure **2(c)** shows that the nanotubes fabricated have periodic rings which presents nanotubes with rough walls this can be attributed to current oscillations [48]. The fabricated nanotubes in an organic electrolyte in this work have shown distinct rings which is in contrast to previous findings [49, 50]. EDX analysis was employed to investigate the elemental composition of TNTs annealed at 350 ºC. EDX analysis of the as synthesized TNTs has confirmed the presence Ti atoms and O atoms which confirms the successful anodization of titanium metal to its TiO_2 by electro-anodization. An additional peak of the C element was

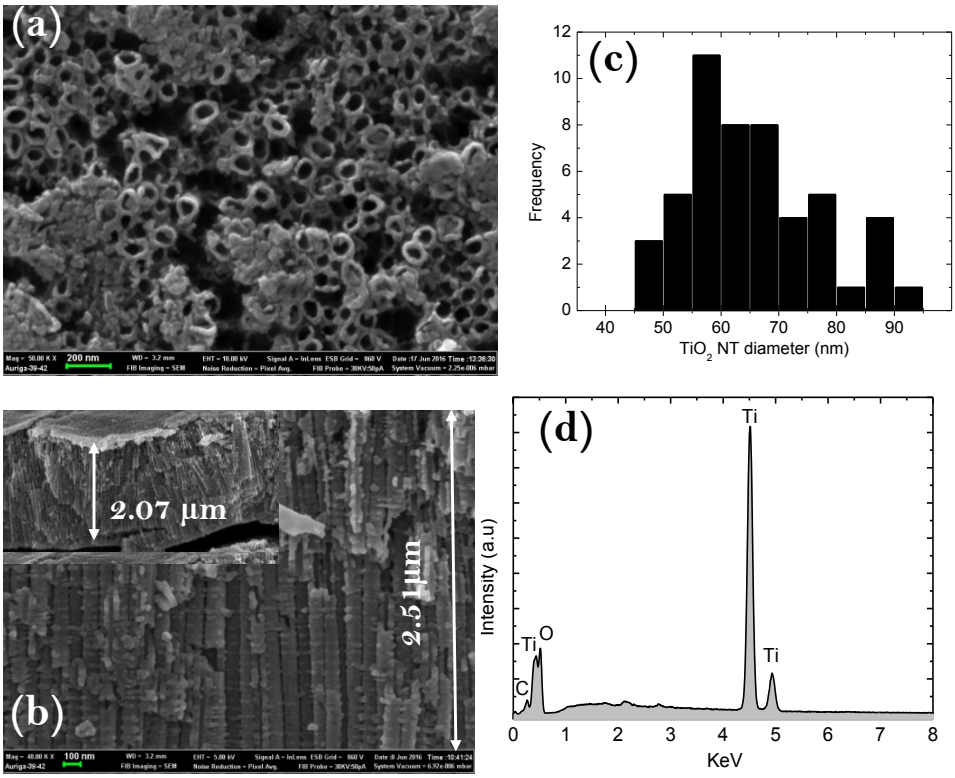

Figure 3: Field-emission scanning electron microscopy (FESEM) images of TNTs annealed at 450 ºC (**a**) surface SEM images of TNTs (**b**) cross sectional SEM images (**c**) Histogram showing pore size distribution (**d**) elemental composition via EDX.

observed in the EDX spectrum at about 2 KeV. The results have confirmed the presence of C species in the anodized TNTs. The main reason being that the carbonaceous species originated from the glycerol electrolyte that got absorbed onto the TNT nanotubes structured during electro anodization. The glycerol was then oxidized to carbonate during the annealing in an oxygen rich environment and the remaining carbon was in cooperated into the TiO_2 structure resulting in the formation of carbon doped TNTs. The EDX spectrum also reveals that the titanium atom has different oxidation states. The EDX spectra show that the titanium (Ti) atom appears at 0.52 KeV, 2.75 KeV, 4.3 KeV and 4.9 KeV. This is due to different binding energies of the core electrons. The first peak of titanium at 0.52 KeV overlapping with oxygen might be due to the high oxidation state of Ti (IV) and other peaks at 4.2, 4.3 and 4.9 KeV are due to titanium in oxidation state of plus three Ti (III). The decline in titanium oxidation state has been ascribed due to carbon doping from the glycerol electrolyte [51].

Increase in annealing temperature from 350 ºC to 450 ºC had no significant effect on the crystalline morphology of the TNTs. In fact, Figure **3(a)** shows that there is retention of TNT porous structure since 450 ºC is the optimum temperature of transformation of amorphous phase of titanium to crystalline Anatase [52-54]. Furthermore, since the TNTs in Figure **3(b)** have a maximum length of 2.51µm, it's increasingly difficult for the tubes in the micrometer range to feel the substrate effect [55-57]. The TNTs annealed at 450 ºC Figure **3** revealed a pore diameter range of 45-100 nm, with modal pore size of 56.52 nm, which is somewhat larger than those annealed at 350 ºC. Increase in annealing temperature resulted in the transformation of the amorphous phase to Anatase which resulted in a well crystallized hence the surface morphology has a more improved structure the highly ordered TNTs.

The surface morphology of TNTs annealed at 550 ºC is shown here in Figure **4(a)**, it can be clearly observed that the increase in annealing temperature resulted in change in surface morphology of TNTs. In contrast to the highly ordered TNTs observed at 350 ºC and 450 ºC increase in temperature results in rupture and collapsing of the TNTs and a decrease in overall pore diameter of the TNTs. The histogram in Figure **4 (b),** has revealed TNTs annealed 550 ºC have a pore diameter range of 30-65 nm which is smaller as compared to the one observed at 350 ºC and 450 ºC in Figure **2(a)** and Figure **3(a)**. Figure **4(a)** clearly reveals

that the surface morphology of the TNTs is significantly affected by the increase in annealing temperature. It has been reported that TNTs grown on Ti substrate, direct annealing to crystallinity results in severe "substrate effects". The Ti substrate which supports the TNTs array greatly influences the crystallization process. In this work increase in annealing temperature from 450ºC to 550ºC has confirmed these observations. Further increase in annealing temperature resulted in a significant decrease in TNTs morphology. This change in surface morphology was due to increase in tube walls and decrease in overall pore size diameter.

Figure **5(a)** shows the surface SEM images of TNTs annealed at 650 ºC. It is evident that increase in

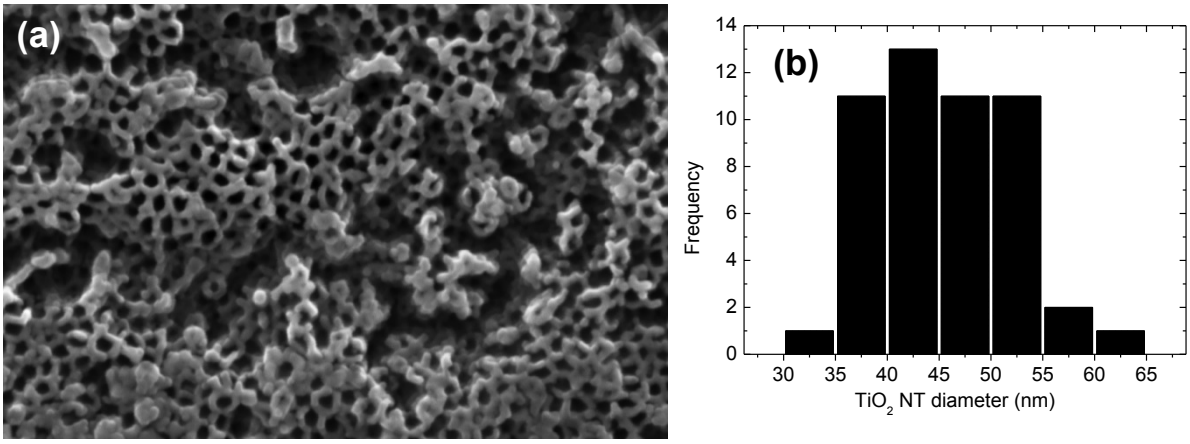

Figure 4: Field-emission scanning electron microscopy (FESEM) images of TNTs annealed at 550 ºC (**a**) surface SEM images of TNTs (**b**) Histogram showing the pore size distribution.

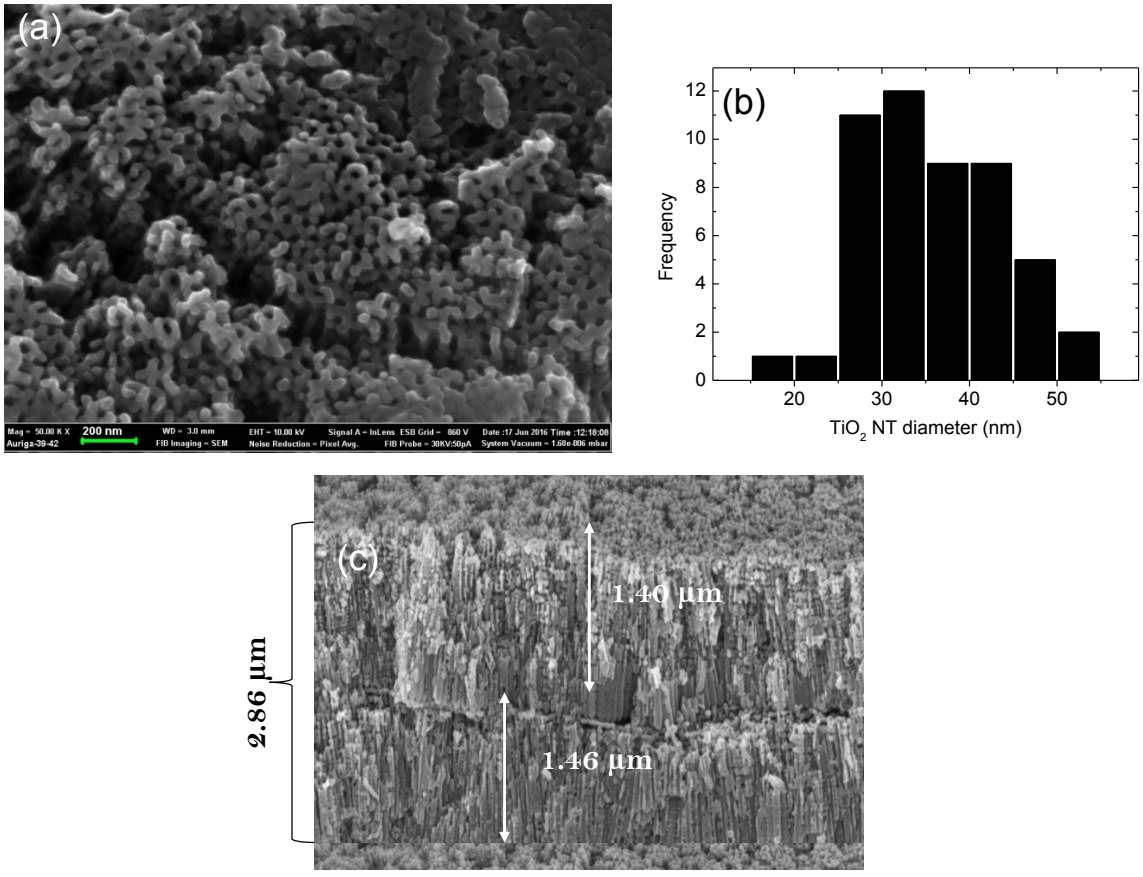

Figure 5: Field-emission scanning electron microscopy (FESEM) images of TNTs annealed at 650 ºC (**a**) Surface SEM images of TNTs (**b**) Cross sectional SEM images (**c**) Histogram showing.

annealing temperature resulted in collapsing and deformation of the TNTs structure. This is accompanied by a decrease in surface area. It has been reported that the increase in annealing temperature results in phase transformation of from Anatase to Rutile phase and this process is catalysed by the presence of Ti substrate. Figure **5(c)**, shows the cross section SEM images of TNTs annealed at 650 ºC which features broken tube bundles, accompanied by dramatically lowered surface area and gradual disappearing of tube structure as the phase transformation from Anatase to Rutile intensified. Figure **5(b)** has revealed a pore diameter range of 15-55 nm, with modal pore size of 31.05 nm which is smaller as compared to the pore size observed at 450 ºC. Hence SEM analysis has revealed that 450 is the ideal annealing temperature for TNTs since at this temperature the annealed samples have improved surface and cross sectional morphology. Moreover they have the largest pore size distribution, which definitely improve the percolation of redox electrolyte onto dye molecules absorbed on the walls of TNTs membranes. Additional the cross sectional analysis have revealed nanotubes with un-deformed tube which will greatly for vectorial transport of photon generated electrons.

3.2. X-Ray Diffraction (XRD) Analysis

Figure **6** shows the XRD patterns of the as anodized and annealed TNT samples on metal substrates at different temperatures from 350 ºC to 650 ºC, in which amorphous regions crystallized to form either Anatase/Rutile phases. The diffraction pattern of the as-anodized showed peaks at 2θ angles of 35.62°, 39.02°, 40.76, 53.55°, 63.49°, 71.14°, and 76.71° revealing only the presence of Ti. There are no peaks of any TiO_2 phases Anatase/Rutile, which indicates that the as-prepared TNTs are amorphous phase. However increase in annealing temperature resulted in the emergence of characteristic peaks for the samples annealed at 350 ºC - 450 ºC at 2θ angles of 24.66º (101) and 27.11º (110) belonging to the Anatase and Rutile phase of TiO_2, respectively.

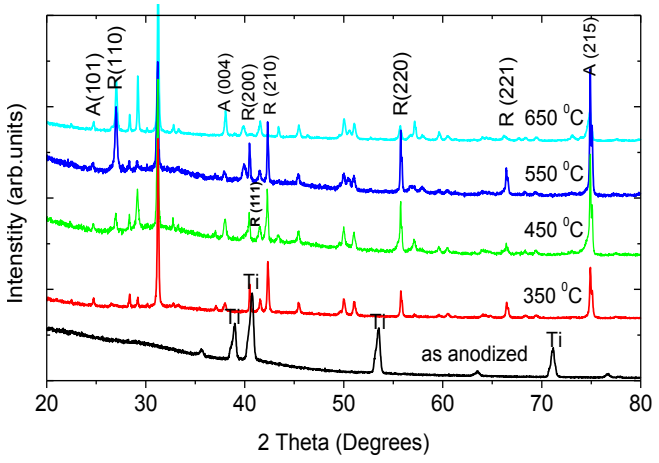

Figure 6: XRD pattern of the TNTs prepared at 60 V in 0.5 wt% NH_4F glycerol electrolyte and annealed at different temperatures.

Furthermore, as the annealing temperature increases from 350 ºC to 550 ºC this results in an increase in the intensity and linewidth of the Anatase peak at 2θ angle of 24.66º (101) increase and decrease. This indicates that increase in annealing temperature results in the improvement of the crystallinity of the sample as the crystallite size decrease. This is a mutual agreement with the SEM images were we observed an improvement in surface morphology of the sample as annealing temperature is increased. Further increase in temperature above 550 ºC to 650 ºC resulted in a decrease in the intensity and linewidth of the characteristic Anatase peak indicating the phase transformation from Anatase to Rutile. This is also in close agreement with SEM surface observations where the structure of the TNTs annealed at 650 ºC completely ruptured and deformed as the temperature increased. The XRD patterns also reveal that as the annealing temperature increases the intensity of characteristic Rutile peak at 27.11º (110) increases at the expense of the Anatase peaks at 2θ angle of 24.66º (101). This indicates that as the annealing temperature increase Rutile of TiO_2 becomes the predominate phase more particularly for TNTs samples on a metal substrate due to accelerated growth of Rutile phase due to the “substrate effect”. To further support these observations in this study, we utilized for the first time Confocal Raman Spectroscopy with correlative image mapping to reveal actual phase changes as the annealing temperature is increased.

3.3. Raman Spectroscopy

3.3.1. Confocal Raman Spectroscopy Large Area Scan CRM -LAS

Raman spectroscopy has been widely employed for the characterization of the electronic structure of TiO_2 nanomaterial. Anatase and Rutile phase of TiO_2 can be sensitively identified by Raman spectroscopy and confocal Raman imaging measurements based on their individual Raman single spectra. Anatase TiO_2 is

characterized the tetragonal space group $D_{4h}^{19}\left(\frac{14}{amd}\right)$ with one primitive unit cell that contains two TiO_2 units with Ti atoms (0, 0, 0) and (0, 1/2, 1/4) and O atoms at (0, 0, u), (0, 0, ū), (0, 1/2, u +1/4) and (0, 1/2, 1/2-u), giving rise to six active Raman modes: A1g + 2B1g + 3Eg, that have been reported in the literature with Raman vibrational frequencies at 144 cm^{-1} (E.g.), 197 cm^{-1} (E.g.), 399 cm^{-1} (B1g), 513 cm^{-1} (A1g), 519 cm^{-1} (B1g), and 639 cm^{-1} (E.g.). Whilst the Rutile counterpart belongs to the P42/mnm tetragonal space group. The unit cell is defined by lattice vectors **a** and **c**, also contains two TiO_2 unit per cell with Ti atoms at (0, 0, 0) and (1/2, 1/2, 1/2) and O ions at ± (u, u, 0) and ± (1/2 +u, 1/2-u, 1/2). The Rutile phase has four Raman vibration modes B1g, Eg, A1g and B2g with Raman vibrational frequencies at around 250 cm^{-1} (B1g), 450 cm^{-1} (Eg), 620 cm^{-1} (A1g) and 826 cm^{-1} (B2g). However, it has been reported in literature that the vibrational frequencies for both Anatase and Rutile phase of TNTs structures to be either blue or red shifted Raman vibrational frequencies as compared to the bulk phases discussed above. Anatase TNTs structures has active Raman vibration modes with the vibrational frequencies at 160.18 cm^{-1}(Eg), 212.51 cm^{-1} (Eg), 399.85 cm^{-1} (B1g), 513. 27 cm^{-1} (A1g) and 631.58 cm^{-1} (Eg) [18]. The shift in the vibrational frequencies has been attributed to phonon confinement caused by a decrease in crystallite size of Anatase TiO_2 nanoparticle Bersani *et al.* [18, 19]. It has been also reported that the highest Eg mode of Anatase TNTs was blue shifted to 631. 65 cm^{-1} whilst the lowest Eg mode was observed to be red shifted by Δ16 cm^{-1}. Figure **7(b)** below shows the typical Raman single spectra recorded at the crosses indicated in the image in Figure **7(a)** with corresponding colour coded spectra. The Raman single spectra (RSS) of the single spot (blue cross in Figure **7(a)**) has revealed that the fabricated TNTs consist of Anatase TiO_2 phase with the vibrational frequencies at 155. 98 cm^{-1} (Eg), 205. 85 cm^{-1} (Eg), 398. 69 cm^{-1}(B1g), 517.32 cm^{-1} (A1g) and 631. 58 cm^{-1} (Eg). The lowest Eg mode in this work has been red shifted by Δ11.98 cm^{-1} whilst the highest Eg mode has been blue shifted by Δ7.42 cm^{-1}. RSS on the single spot highlighted by the pink cross (Figure **7a**) has shown that TNTs consist of a mixed Anatase and Rutile phase with the vibrational frequencies at 157. 43 cm^{-1} Eg(A), 264.91 cm^{-1} Eg(A), 413.95 cm^{-1} Eg(R) and 610.28 cm^{-1} A1g(R). To further scrutinize the morphological distribution of the Anatase and Rutile phase of TiO_2 we performed a large area scan (LAS) on the stitching image (500 µm x 500 µm) to obtain a conclusive phase distribution on the surface of TNTs annealed at 350 ºC covering a large area of the sample. Confocal Raman Imaging LAS was done on the highlighted square area of 330 µm x 330 µm shown here in Figure **7(a-d)** shows the corresponding draw images from basis analysis. This resulted in a colour coded combined image that consists of four different colours which corresponds to the coloured coded spectra obtained from basis analysis shown here in Figure **7(f)** with corresponding colour coded spectra in Figure **7(g).** Figure **7(g)** gives a conclusive distribution of the TiO_2 phases over a large area of a sample of TNTs annealed at 350 ºC. It is clearly evident from Figure **7(g)** that more than one phase TiO_2 exist over a large area of the sample scanned. The blue area with corresponding colour coded Raman Spectra in Figure **7(g)** shows that the majority of the TNTs sample annealed at 350 ºC consist of Anatase phase of TiO_2 with Raman vibration frequencies at 157.47 cm^{-1} (Eg), 205.85 cm^{-1} (Eg), 399.65 cm^{-1} (B1g), 518. 01 cm^{-1} (A1g) and 639.17 cm^{-1} (Eg). Whilst the grey with corresponding color coded spectra in Figure **7(g)** consist of a mixed Anatase and Rutile phase with Raman vibration frequencies at 157.66 cm^{-1} Eg(A), 209.64 cm^{-1} Eg(A), 267.03 cm^{-1} B1g(R), 413.46 cm^{-1} Eg(R) and 613.04 cm^{-1} A1g(R). Whilst the green area with corresponding color coded Raman spectra has Raman vibration modes at 155.01 cm^{-1} (Eg), 208.02 cm^{-1} (Eg), 402.49 cm^{-1} (B1g), 517.90 cm^{-1} (A1g) and 636.81 cm^{-1} (Eg) all belonging to the Anatase phase of TiO_2. Whilst the pink spotted area has Raman vibrational modes at 160.48 cm^{-1} (Eg), 398, 98 cm^{-1} (B1g) and 623.95 cm^{-1} (Eg) reveals the Raman modes of a vaguely detected Anatase phase. The broadness of the peaks can be related to the degree of crystallinity of the Anatase oxide and smaller crystallite size of the nanotube walls. The Raman spectra of the strongest well resolved Eg vibrational mode at 160.48 cm^{-1} has a FWHM of 20.28 cm^{-1} whilst the bulk Anatase phase with strongest has a FWHM of 25.4 cm^{-1} Degussa P25 with modal particle size of 25 nm. Our Confocal Raman large area measurements outperform single spot RSS measurements that have been reported in the literature as our measurements have given a conclusive TNTs phase distribution over a larger sample area. In addition these measurements have outperformed observations from XRD analysis which do not reveal the exact location of TiO_2 phase on sample which key in development of efficient electrode material for DSSC.

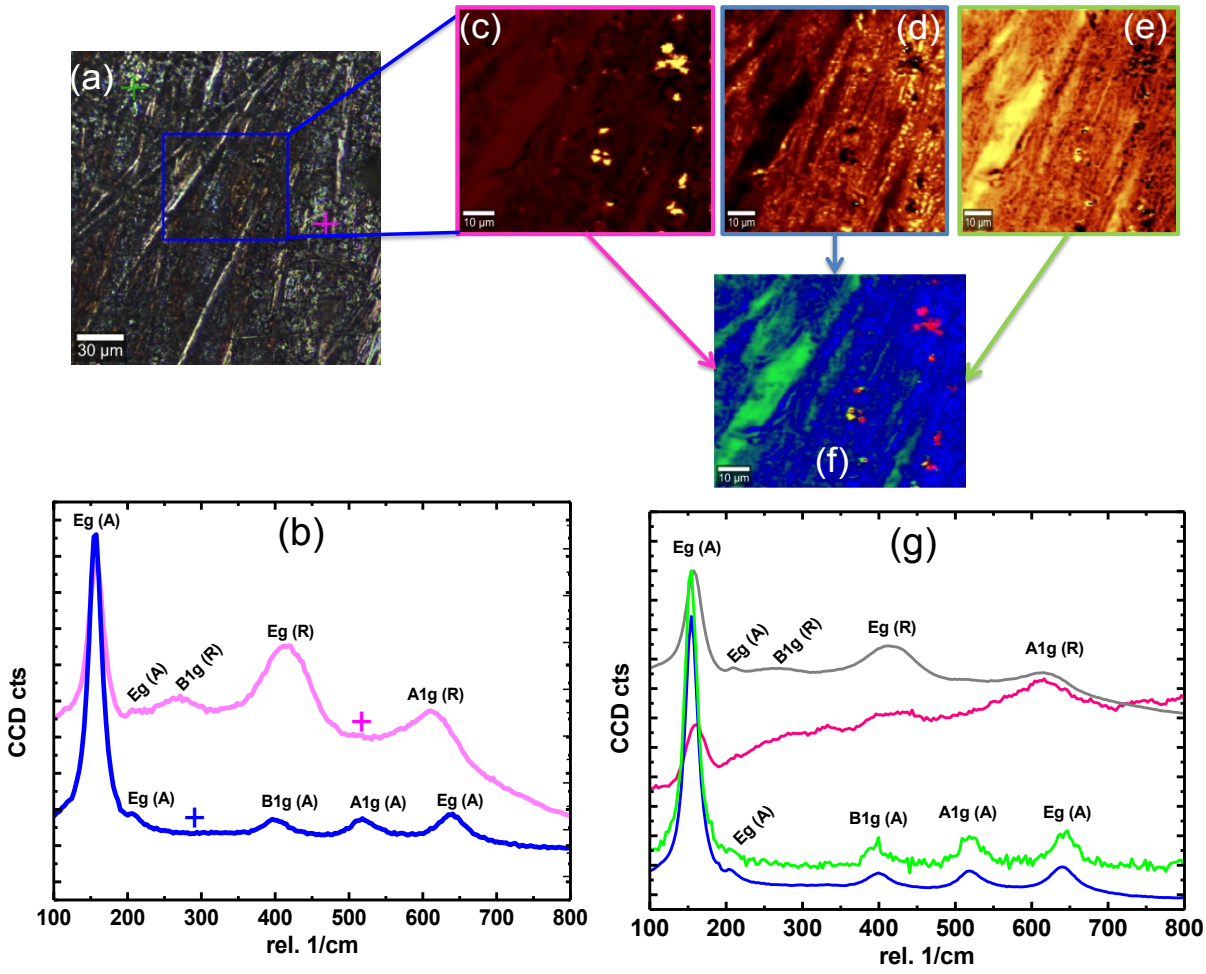

Figure 7: Shows large area scan of TNTs annealed at 350 ºC (**a**) stitching image (**b**) Raman single spectra recorded at the crosses indicated in the image in (**a**) with corresponding colours, (**c**), (**d**), and (**e**) draw image from resulting showing phase distribution of TiO_2 following basis analysis. Brighter colours indicate a higher fitting factor and thus higher signal intensity of the corresponding spectrum at that position (**f**) combined image of three different spectra indicating existence of three different phases at the surface of the TNTs pink spots=less crystallized Anatase phase, blue area=well crystallized Anatase phase, cyan area well crystallized Anatase phase grey area indicating the existence of mixed Anatase and Rutile Phases (**g**) shows the corresponding color coded spectra of (**f**).

Figure **8** shows the confocal Raman Large area of TNTs annealed at 450 ºC. Figure **8(a)** shows stitching image of an area 500 µm x 500 µm. Confocal Raman Imaging LAS which was performed in the highlighted red square area 330 µm x 330 µm (Figure **8a**) and the corresponding draw image from basis analysis shown in Figure **8(c-e)** reveal the presence of only of three distinct phases of TNTs. Figure **8(b)** reveals that RSS single spot measurements of the red and blue have vibrational modes at 156.41 cm^{-1} (Eg), 206.21 cm^{-1} (Eg), 399.30 cm^{-1} (B1g), 518.25 (A1g) and 639.51 cm^{-1} (Eg) all belonging to a well crystallized Anatase phase of TiO_2. On combining the two draw images in Figure **8(c)** and **(d)** resulted in a combined colour code bitmap image of that gives a conclusive phase distribution with the corresponding colour coded spectra in Figure **8(f)**. Figure **8(f)** revealed that TNTs sample consists of Raman spectra for the blue and red area have Raman vibration modes at 156.41 cm^{-1} (Eg), 206.21 cm^{-1} (Eg), 399.30 cm^{-1} (B1g), 518.25 cm^{-1} (A1g) and 639.51 cm^{-1} (Eg) all belonging to Anatase phase of TiO_2. Additionally the grey area highlighted by the bright spots in draw image Figure **8(e)** has revealed Raman mixed Anatase and Rutile phase with Raman vibrational modes at 153. 71 cm^{-1} Eg(A), 252.96 cm^{-1} B1g(R), 439.18 cm^{-1} Eg(R), and 614.90 cm^{-1} A1g(R) as depicted in grey spectra in Figure **8(f)**. However the result show a mixed Anatase to Rutile area which consisted of only a small percentage of the whole sample. It has been reported that the presence of a

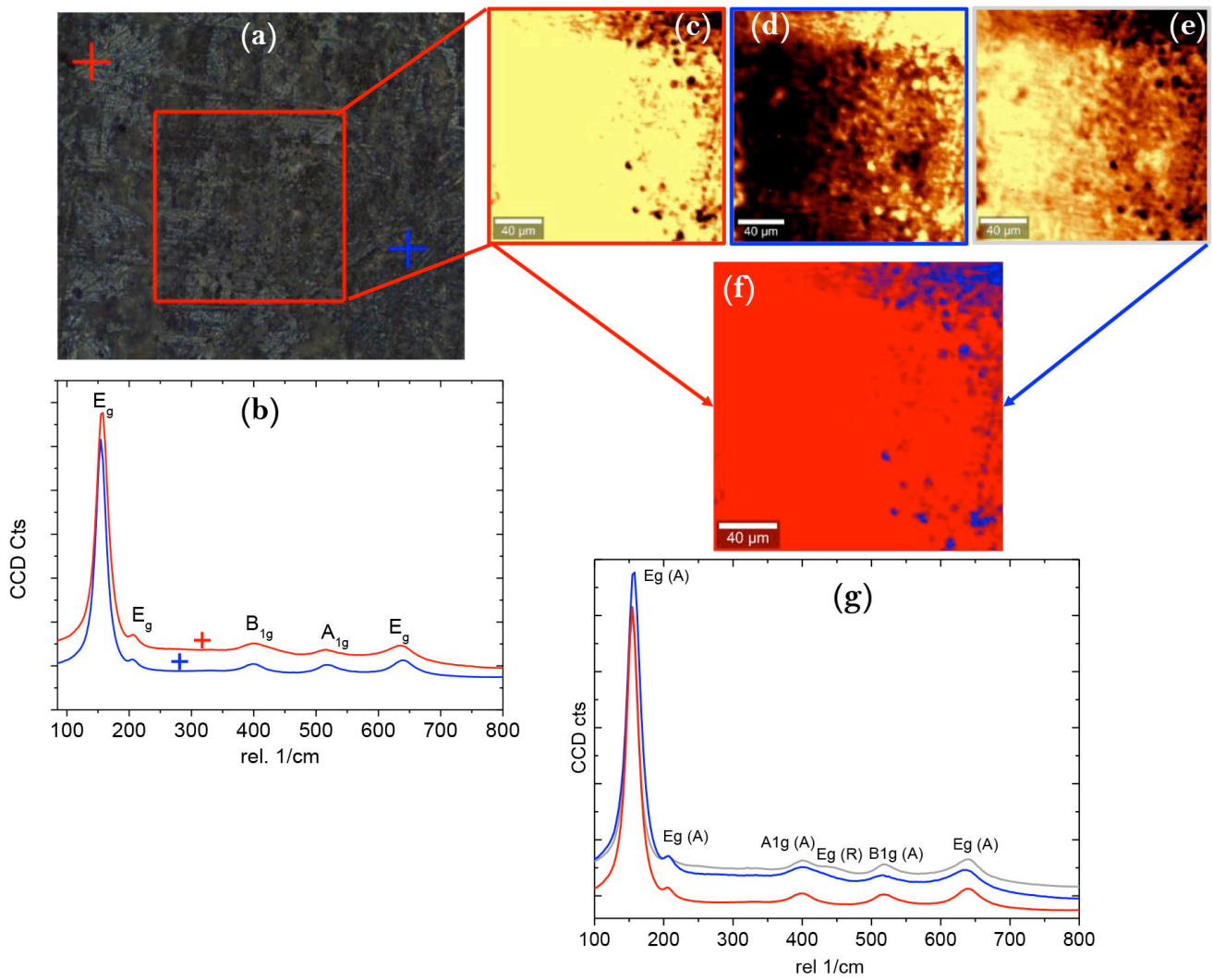

Figure 8: Shows large area scan of TNTs annealed at 450 ºC (**a**) stitching image (**b**) Raman single spectra recorded at the crosses indicated in the image in (**a**) with corresponding colours. (**c**), and (**d**) Resulting draw images showing phase distribution of TiO_2 following basis analysis. (**e**) Combined image spectra indicating existence of one phase of TiO_2 (**f**) shows the corresponding colour coded spectra of (**e**).

small amounts of rutile phase within the majority Anatase phase significantly improves the efficiency of the photo electrodes for photo catalysis this is attributed to improved grain size, and connections between grain boundaries which decrease electron-hole recombination [20-22]. It is apparent that with increase in annealing temperature from 350 ºC to 450 ºC resulted in a significant narrowing of the strongest well resolved Eg vibrational mode and corresponding peak intensities increased. This implies that the crystallinity was greatly enhanced by raising the annealing temperatures [23, 24]. This in agreement with SEM observations that showed TNTs annealed at 450 ºC which had improved pore size distribution as well as the morphology. Confocal Raman mapping in this work allowed us to closely monitor the phase changes in the investigated sample and correlate it to change in morphology from SEM analysis. We can clearly observed that the TNTs annealed at 450 ºC had a dominate Anatase phases, Moreover the Anatase phases is accompanied by traces of Rutile phase, which improved the morphology of TNTs annealed at 450 ºC as supported by the SEM images in Figure **3**.

To further investigate the effect of increase in annealing temperature and correlate our finding with the significant change surface morphology of TNTs annealed at 650 ºC. SEM analysis revealed that the TNTs annealed 650 ºC (Figure **5**) collapsed and deformed as the annealing temperature increases. We also performed confocal Raman large area scan for the TNTs samples annealed at 650 ºC and findings are shown here in Figure **9**.

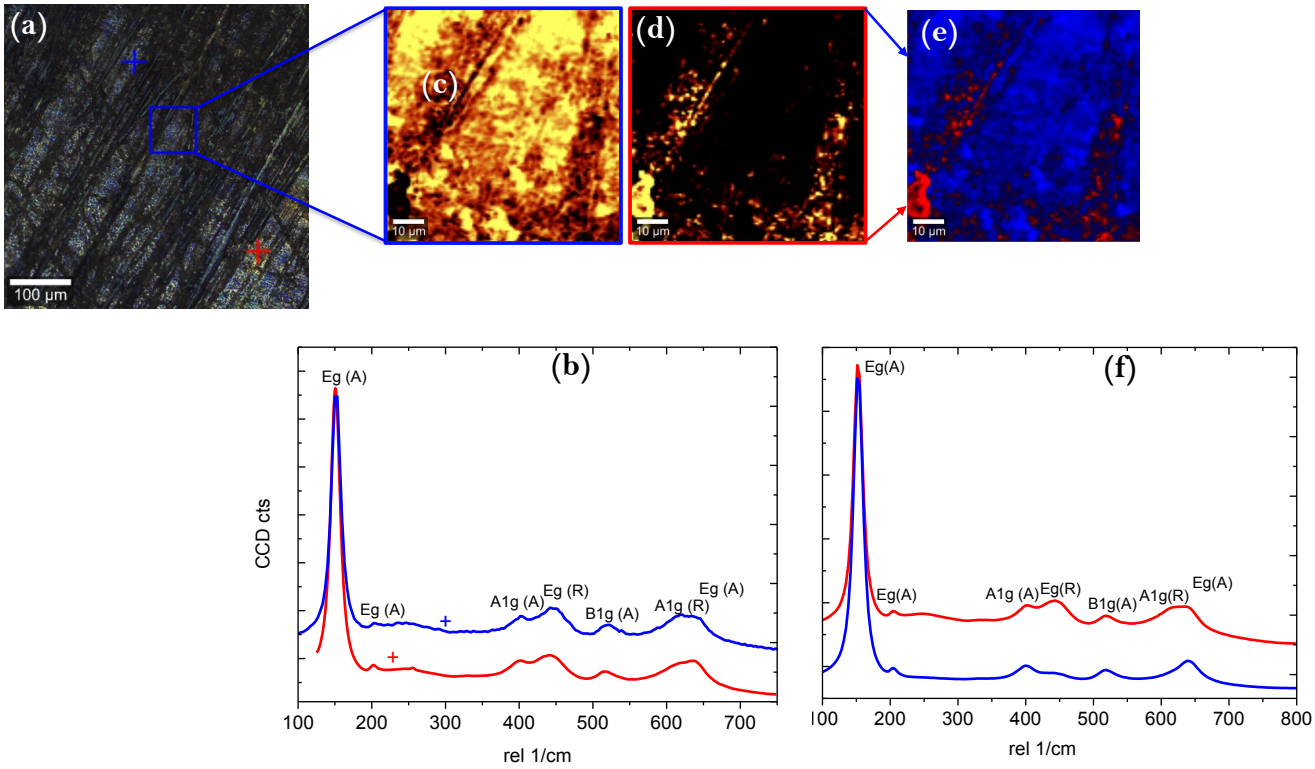

Figure 9: Shows large area scan of TNTs annealed at 650 ºC (**a**) Stitching image (**b**) Raman single spectra recorded at the crosses indicated in the image in (**a**) with corresponding colours, (**c**) and (**d**) draw image showing phase distribution of TiO_2 following basis analysis. Brighter colours indicate a higher fitting factor and thus higher signal intensity of the corresponding spectrum at that position (**e**) combined image of (**f**) shows the corresponding colour coded spectra.

Raman single spectra from the crosses in Figure **9(a)** shown here in Figure **9(b)** have revealed Raman vibration modes at 152.79 cm^{-1} Eg (A), 205.04 cm^{-1} Eg(A), 404.97 cm^{-1} A1g(A), 441.09 cm^{-1} Eg(R), 519.37 cm^{-1} B1g(A), 617.91 cm^{-1} A1g(R), and 629.34 cm^{-1} Eg(A) all belonging to mixed Anatase to Rutile phase. Moreover Raman mapping following basis analysis over a large area scan Figure **9(e)**, has shown the annealed sample consist of a mixed Anatase and Rutile phase as illustrated here in Figure **9(f)**. The TNTs phases of the weight percentage composition of Rutile to Anatase from the integrated peak intensity of the Rutile peak of TNTs annealed at 650 following the linear relation in Eq. (**3**). Following the Rutile peak at 441.09 cm^{-1} and the Anatase peak at 404.97 cm^{-1} has revealed a 65 % weight ratio.

3.2. Confocal Raman Spectroscopy Depth Scan

To finally evaluate the effect of annealing temperature on structural properties of TNTs membranes we performed a confocal Raman Depth Scan. Figure **10** here shows a color coded confocal Raman depth scan performed on TNTs membranes annealed at 650 ºC. Confocal Raman image depth profiling the sample has revealed a mixed Anatase and Rutile phase, with vibration modes at for the red coded spectra in the combined bitmap in Figure **10(e)**. 152.17 cm^{-1}, 201.87 cm^{-1}, 401.60 cm^{-1}, 440.60 cm^{-1} , 519.18 cm^{-1} and 619.59 cm^{-1}. It has been that due to the substrate effect the Rutile to Anatase growth start from the underlying titanium metal substrate. Furthermore the TNTs membranes are gradually densified from the metal substrate/TNTs membrane interface which is accompanied by lowered surface area and gradually disappearing tube structure. This is in agreement with SEM images shown here in Figure **5**. Where we observed complete deformation of TNTs structure.

3.3. Atomic Force Microscopy (AFM)

Figure **11** shows the AFM images of TNTs membranes annealed at different temperatures. The bright yellow colour represents the walls of the tubes while darker yellow represents pores. 3D AFM surface topography images were used in this study to support SEM images observations. AFM analysis has revealed an increase in annealing temperature results in a change in the surface topography of the TNTs

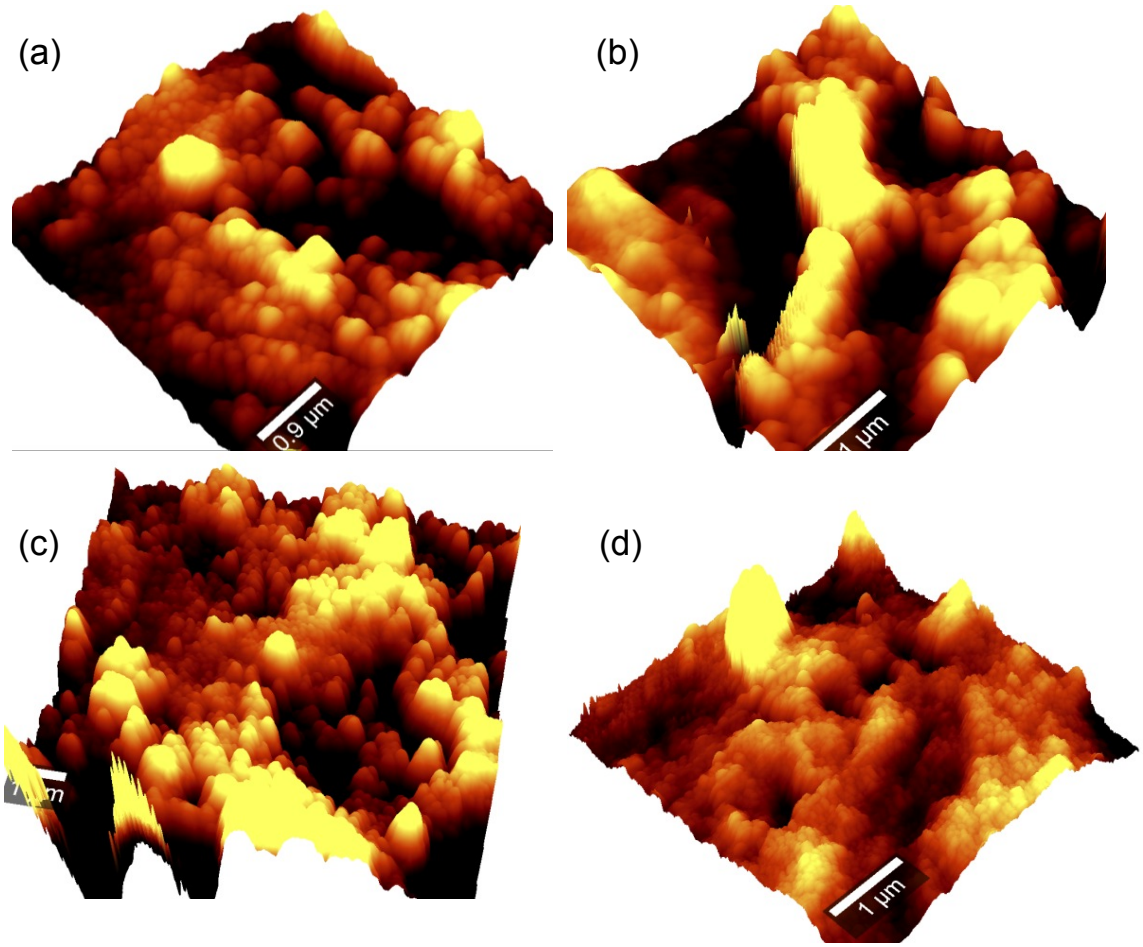

Figure 11: Shows 3D AFM-picture of surface topography of TNTs membranes annealed at (**a**) 350 ºC, (**b**) 450 ºC (**c**) 550 ºC and 650 ºC.

membranes. AFM analysis has shown that the TNTs membranes have a porous structure which is in a relatively good agreement with SEM analysis.

4. CONCLUSIONS

Highly ordered TNTs membranes have been synthesized by an electro anodization technique employing a glycerol electrolyte solution 0.5 wt% NH_4F at room temperature at 60 V. SEM analysis has revealed the change in morphology with increase in annealing temperature. SEM analysis revealed that the TNTs annealed 650 ºC collapsed and deformed as the annealing temperature increased. This was in mutual agreement with XRD analysis, which revealed that as the annealing temperature increased the intensity of characteristic Rutile peak at 27.11º (110) increases at the expense of the Anatase peaks at 2θ angle of 24.66º (101). Large area scan confocal Raman microscopy measurements have revealed Raman vibration modes at 152.79 cm^{-1} Eg (A), 205.04 cm^{-1} Eg(A), 404.97 cm^{-1} A1g(A), 441.09 cm^{-1} Eg(R), 519.37 cm^{-1} B1g(A), 617.91 cm^{-1} A1g(R), and 629.34 cm^{-1} Eg(A) all belonging to mixed Anatase to Rutile phase with a 65 % weight ratio. AFM surface topography has revealed the presence of porous structure which supported SEM observations. Overally our method of characterizing Titanium dioxide nanotube membranes from the large area scans on the surface of samples and to depth profiling along the tube of the membranes using confocal Raman spectroscopy may prove to be key step in development of efficient electrode materials of solar devices. The confocal Raman Spectroscopy provided in detailed the phase variation on the surface of the nanotubes and also phase variations along the nanotubes.

ACKNOWLEDGMENTS

We are grateful for financial support from our sponsors' South African National research foundation (NRF), Govan Mbeki Research and Development Centre (GMRDC) of the University of Fort Hare and Sasol Inzalo Foundation. The authors we also like to

acknowledge the DST/CSIR Nanotechnology Innovation Centre, National Centre for Nanostructured Materials, CSIR characterization of the TiO_2 nanotubes samples.

REFERENCES

[1] D. Kuang, J. Brillet, P. Chen, M. Takata, S. Uchida, H. Miura, K. Sumioka, S.M. Zakeeruddin, M. Grätzel. Application of highly ordered TiO_2 nanotube arrays in flexible dye-sensitized solar cells. ACS Nano 2008; 6: 1113-1136. https://doi.org/10.1021/nn800174y

[2] A. Ghicov, S.P. Albu, R. Hahn, D. Kim, T. Stergiopoulos, J. Kunze, *et al.* TiO_2 Nanotubes in Dye-Sensitized Solar Cells: Critical Factors for the Conversion Efficiency. Chem Asian J 2009; 4: 55-60. https://doi.org/10.1002/asia.200800441

[3] P. Roy, D. Kim, K. Lee, E. Spiecker, P. Schmuki. TiO_2 nanotubes and their application in dye-sensitized solar cells. Nanoscale 2010; 2: 45. https://doi.org/10.1039/B9NR00131J

[4] J. Lin, M. Guo, C.T. Yip, W. Lu, G. Zhang, X. Liu, *et al.* High temperature crystallization of free-standing Anatase TiO_2 nanotube membranes for high efficiency dye-sensitized solar cells. Adv Funct Mat 2013; 23: 5952. https://doi.org/10.1002/adfm.201301066

[5] J.M. Macak, H. Tsuchiya, A. Ghicov, K. Yasuda, R. Hahn, S. Baver, *et al.* TiO_2 nanotubes: Self-organized electrochemical formation, properties and applications. Curr Opin Solid State Mat Sci 2007; 11: 3-18. https://doi.org/10.1016/j.cossms.2007.08.004

[6] K. Shankar, J.I. Basham, N.K. Allam, O.K. Varghese, G.K. Mor, X.J. Feng, *et al.* Grimes, Is it effective to harvest visible light by decreasing the band gap of photocatalytic materials? J Phys Chem C 2009; 113: 6327. https://doi.org/10.1021/jp809385x

[7] N.K. Allam, M.A. EI-Sayed. Photoelectrochemical water oxidation characteristics of anodically fabricated TiO_2 nanotube arrays: Structural and optical properties. J Phys Chem C 2010; 112: 12687.

[8] H.I. Hsiang, S.C. Lin. Effects of aging on the phase transformation and sintering properties of TiO_2 gels. Mater Sci Eng A 2004; 380: 67-72. https://doi.org/10.1016/j.msea.2004.03.045

[9] H.I. Hsiang, S.C. Lin. Effects of aging on nanocrystalline anatase-to-rutile phase transformation kinetics, Ceram. Ceram Int 2008; 34: 557-561. https://doi.org/10.1016/j.ceramint.2006.12.004

[10] M. Qamar, C.R. Yoon, H.J. Oh, N.H. Lee, K. Park, D.H. Kim, *et al.* Preparation and photocatalytic activity of nanotubes obtained from titanium dioxide. J Catal Today 2008; 131: 3-14. https://doi.org/10.1016/j.cattod.2007.10.015

[11] L. Kevan, B. O'Regan, A. Kay, M. Gratzel. Preparation of TiO_2 (anatase) films on electrodes by anodic oxidative hydrolysis of $TiCl_3$. J Electroanal Chem 1993; 346: 291. https://doi.org/10.1016/0022-0728(93)85020-H

[12] A. Sedghi, H.N. Miankushki. Influence of TiO_2 electrode properties on performance of dye-sensitized solar cells. Int J Electrochem Sci 2012; 7: 12078.

[13] M.K. Nazeeruddin, A. Kay, I. Rodicio, R. Humpbry-Baker, E. Miiller, P. Liska, *et al.* Conversion of light to electricity by cis-X2bis(2,2'-bipyridyl-4,4'-dicarboxylate)ruthenium(II) charge-transfer sensitizers (X=Cl-, Br-, I-, CN-, and SCN-) on nanocrystalline titanium dioxide electrodes. J Am Chem Soc 1993; 115: 6382. https://doi.org/10.1021/ja00067a063

[14] N.G. Park, G. Schlichthrl, J. van de Lagemaat, H.M. Cheong, A. Mascarenhas, A.J. Frank. Dye-sensitized TiO_2 solar cells: Structural and photoelectrochemical characterization of nanocrystalline electrodes formed from the hydrolysis of $TiCl_4$. J Phys Chem B 1999; 103: 3308. https://doi.org/10.1021/jp984529i

[15] S. Ito, P. Liska, P. Comte, R. Charvet, P. Pechy, U. Bach, L, *et al.* Control of dark current in photoelectrochemical (TiO_2/I-I3) and dye-sensitized solar cells. Chem Commun 2005; 4351. https://doi.org/10.1039/b505718c

[16] P.M. Sommeling, B.C. O'Regan, R.R. Haswell, H.J.P. Smit, N.J. Bakker, J.J.T. Smits, *et al.* Influence of a $TiCl_4$ post-treatment on nanocrystalline TiO_2 films in dye-sensitized solar cells. J Phys Chem B 2006; 110: 19191. https://doi.org/10.1021/jp061346k

[17] B.C. O'Regan, J.R. Durrant, P.M. Sommeling, N.J. Bakker. Influence of the $TiCl_4$ Treatment on Nanocrystalline TiO_2 Films in Dye-Sensitized Solar Cells. 2. Charge density, band edge shifts, and quantification of recombination losses at short circuit. J Phys Chem C 2007; 111: 14001. https://doi.org/10.1021/jp073056p

[18] C.T. Yip, C.S.K. Mak, A.B. Djurisic, Y.F. Hsu, W.K. Chan. Dye-sensitized solar cells based on TiO_2 nanotube/porous layer mixed morphology. Appl Phys A 2008; 92: 589. https://doi.org/10.1007/s00339-008-4624-x

[19] C.J. Barbe, F. Arendse, P. Comte, M. Jirousek, F. Lenzmann, V. Shklover, *et al.* Nanocrystalline Titanium Oxide electrodes for photovoltaic applications. J Am Ceram Soc 1997; 80: 3157. https://doi.org/10.1111/j.1151-2916.1997.tb03245.x

[20] Khan SUM, M. Al-Shahry, W.B. Jr Ingler WB. Efficient photochemical water splitting by a chemically modified n-TiO_2. Science 2002; 297: 2243. https://doi.org/10.1126/science.1075035

[21] Asahi R, Morikawa T, Ohwaki T, Aoki K, Taga Y. Visible-light photocatalysis in nitrogen-doped titanium oxides. Science 2001; 293: 269. https://doi.org/10.1126/science.1061051

[22] R.P. Vitiello, J.M. Macak, A. Ghicov, H. Tsuchiya, L.F.P. Dick, P. Schmuki. N-Doping of anodic TiO_2 nanotubes using heat treatment in ammonia. Electrochem Commun 2006; 8: 544. https://doi.org/10.1016/j.elecom.2006.01.023

[23] R. Ghicov, J.M. Macak, H. Tsuchiya, J. Kunze, V. Haeublein, L. Frey, P. Schmuki. Ion implantation and annealing for an efficient N-doping of TiO_2 nanotubes. Nano Lett 2006; 6: 1080. https://doi.org/10.1021/nl0600979

[24] A.L. Kontos, A.G. Kontos, Y.S. Raptis, P. Falaras. Nitrogen modified nanostructured titania: Electronic, structural and visible-light photocatalytic properties. Phys Status Solidi RRL 2008; 2: 83. https://doi.org/10.1002/pssr.200802006

[25] T. Umebayashi, T. Yamaki, K. Asai. Band gap narrowing of titanium dioxide by sulfur doping. Appl Phys Lett 2002; 81: 454. https://doi.org/10.1063/1.1493647

[26] T. Yamaki, T. Sumita, S. Yamamoto. Formation of TiO_{2-xFx} compounds in fluorine-implanted TiO_2. J Mat Sci Lett 2002; 21: 33. https://doi.org/10.1023/A:1014282225859

[27] G.J. Ren, Y. Gao, X. Liu, A. Xing, H.T. Liu, J.G. Yin. Synthesis of high-activity F-doped TiO_2 photocatalyst via a simple one-step hydrothermal process. React Kinet Mech Catal 2010; 100: 487. https://doi.org/10.1007/s11144-010-0194-y

[28] N. Al-salim, S.A. Bagshaw, A. Bittar, T. Kemmitt, A.J. McQuillan, A.M. Mills, *et al.* Characterisation and activity of sol-gel-prepared TiO_2 photocatalysts modified with Ca, Sr or Ba ion additives. J Mat Chem 2000; 10: 2358. https://doi.org/10.1039/b004384m

[29] M. Kang. Synthesis of Fe/TiO_2 photocatalyst with nanometer size by solvothermal method and the effect of H_2O addition on structural stability and photodecomposition of methanol. J Mol Catal A 2003; 197: 173. https://doi.org/10.1016/S1381-1169(02)00586-1

[30] K. Wilke, H.D. Breuer. The influence of transition metal doping on the physical and photocatalytic properties of titania. J Photochem Photobiol A 1999; 121: 49. https://doi.org/10.1016/S1010-6030(98)00452-3

[31] J. Wang, S. Uma, K.J. Klabunde. Visible light photocatalysis in transition metal incorporated titania-silica aerogels. Appl Catal B Environ 2004; 48: 151. https://doi.org/10.1016/j.apcatb.2003.10.006

[32] Y. Yang, X.J. Li, J.T. Chen, L.Y. Wang. Effect of doping mode on the photocatalytic activities of Mo/TiO_2. J Photochem Photobiol A 2004; 163: 517. https://doi.org/10.1016/j.jphotochem.2004.02.008

[33] A.W. Xu, Y. Gao, H.Q. Liu. The preparation, characterization, and their photocatalytic activities of rare-earth-doped TiO_2 Nanoparticles. J Catal 2002; 207: 151. https://doi.org/10.1006/jcat.2002.3539

[34] F. Mohammadpour, M. Altomare, S. So, K. Lee, M. Mokhtar, A. Alshehri, P. Schmuki. High-temperature annealing of TiO_2 nanotube membranes for efficient dye-sensitized solar cells. Semicond Sci Tech 2016; 31: 014010. https://doi.org/10.1088/0268-1242/31/1/014010

[35] K. Zhu, N.R. Neale, A. Miedaner, A.J. Frank. Enhanced charge-collection efficiencies and light scattering in dye-sensitized solar cells using oriented TiO_2 nanotubes arrays. Nano Lett 2007; 7: 69. https://doi.org/10.1021/nl062000o

[36] C. Richter, C.A. Schmuttenmaer. Schmuttenmaer, Exciton-like trap states limit electron mobility in TiO_2 nanotubes. Nature Nanotech 2010; 5: 769. https://doi.org/10.1038/nnano.2010.196

[37] J.R. Jennings, A. Ghicov, L.M. Peter, P. Schmuki, A.B. Walker. Walker, Dye-sensitized solar cells based on oriented TiO_2 nanotube arrays: Transport, trapping, and transfer of electrons. J Am Chem Soc 2008; 10: 13364. https://doi.org/10.1021/ja804852z

[38] P. Roy, D. Kim, K. Lee, E. Spiecker, P. Schmuki. TiO_2 nanotubes and their application in dye-sensitized solar cells. Nanoscale 2010; 2: 45. https://doi.org/10.1039/B9NR00131J

[39] J. Choi, S.H. Park, Y.S. Kwon, J. Lim, I.Y. Song, T. Park, Facile fabrication of aligned doubly open-ended TiO_2 nanotubes, via a selective etching process, for use in front-illuminated dye sensitized solar cells (Communication). Chem. Commun 2012; 48: 8748. https://doi.org/10.1039/c2cc33629d

[40] Y. Yu, K. Wu, K. She, D. Wang, D. Dye stability of dye-sensitized solar cells with a conducting and a non-conducting electrode. Eur Phys J Appl Phys 2013; 61: 10201. https://doi.org/10.1051/epjap/2012120185

[41] J. Martin, S.G. Hirsch, A. Giri, M.H. Griep, S.P. Karna, Nanotechnology (IEEE-NANO) (2012), 12th IEEE Conference.

[42] Regonini, C.R. Bowen, A. Jaroenworaluck, R. Stevens. A review of growth mechanism, structure and crystallinity of anodized TiO_2 nanotubes. Mat Sci Eng R: Rep 2013; 74: 377. https://doi.org/10.1016/j.mser.2013.10.001

[43] P. Roy, S. Berger, P. Schmuki. TiO_2 nanotubes: Synthesis and applications. Angewandte Chemie - International Edition 2011; 50(13): 2904-2939. https://doi.org/10.1002/anie.201001374

[44] G. Liu, K. Wang, N. Hoivik, H. Jakobsen. Progress on free-standing and flow-through TiO_2 nanotube membranes. Solar Energy Materials and Solar Cells 2012; 98: 24. https://doi.org/10.1016/j.solmat.2011.11.004

[45] S.M. Bhosle, R. Tewari, C.R. Friedrich. Dependence of nanotextured titanium orthopedic surfaces on electrolyte condition. J Surf Eng Mat Adv Tech 2016; 6: 164. https://doi.org/10.4236/jsemat.2016.64015

[46] V. Galstyan, E. Comini, G. Faglia, G. Sberveglieri. TiO_2 nanotubes: Recent advances in synthesis and gas sensing properties. Sensors (Basel, Switzerland) 2013; 13(11): 14813-14838. https://doi.org/10.3390/s131114813

[47] Y.J. Park, J.M. Ha, G. Ali, H.J. Kim, Y. Addad, S.O. Cho. Controlled fabrication of nanoporous oxide layers on zircaloy by anodization. Nanoscale Res Lett 2015; 10(1): 377. https://doi.org/10.1186/s11671-015-1086-x

[48] Y. Li, H. Yu, C. Zhang, W. Song, G. Li, Z. Shao, B. Yi. Effect of water and annealing temperature of anodized TiO_2 nanotubes on hydrogen production in photoelectrochemical cell. Electrochim Acta 2013; 107: 313-319. https://doi.org/10.1016/j.electacta.2013.05.090

[49] J. Macák. Growth of anodic self-organized titanium dioxide nanotube layers. 2008; 1-168. http://www.opus.ub.unierlangen.de/opus/volltexte/2008/935/

[50] J.M. Macak, S.P. Albu, P. Schmuki. Towards ideal hexagonal self-ordering of TiO_2 nanotubes. Phys Status Solidi RRL 2007; 1: 181-183. https://doi.org/10.1002/pssr.200701148

[51] S.P. Albu, A. Ghicov, J.M. Macak, P. Schmuki. 250 μm long anodic TiO_2 nanotubes with hexagonal self-ordering. Phys Status Solidi RRL 2007; 1: 65-67. https://doi.org/10.1002/pssr.200600069

[52] Q. Zhu, Y. Peng, L. Lin, C.M. Fan, G.Q. Gao, R.X. Wang, A.W Xu. Stable blue TiO_{2-x} nanoparticles for efficient visible light photocatalysts. J Mat Chem A 2014; 2: 4429. https://doi.org/10.1039/c3ta14484d

[53] Z. Lockman, C.H. Kit, S. Sreekantan. Effect of annealing temperature on the Anatase and Rutile TiO_2 nanotubes formation. J Nucl Tech 2009; 6(1): 57-64.

[54] Y. Liu, X. Zhang. Effect of calcination temperature on the morphology and electrochemical properties of Co_3O_4 for lithium-ion battery. Electrochim Acta 2009; 54(17): 4180-4185. https://doi.org/10.1016/j.electacta.2009.02.060

[55] A. Jaroenworaluck, D. Regonini, C.R. Bowen, R. Stevens. A microscopy study of the effect of heat treatment on the structure and properties of anodised TiO_2 nanotubes. Appl Surf Sci 2010; 256(9): 2672-2679. https://doi.org/10.1016/j.apsusc.2009.09.078

[56] S.P. Albu, H. Tsuchiya, S. Fujimoto, P. Schmuki. TiO_2 nanotubes–Annealing effects on detailed morphology and

structure. Eur J Inorg Chem 2010; 27: 4351-4356. https://doi.org/10.1002/ejic.201000608

[57] S. Leonardi, V. Russo, A. Li Bassi, F. Di Fonzo, T.M. Murray, H. Efstathiadis, J. Kunze-Liebhäuser. TiO_2 nanotubes: Interdependence of substrate grain orientation and growth rate. ACS Appl Mat Inter 2015; 7(3): 1662-1668. https://doi.org/10.1021/am507181p

Received on 02-11-2016 Accepted on 12-01-2017 Published on 20-03-2017

DOI: http://dx.doi.org/10.15377/2410-4701.2016.03.02.3